Analytical and Bioanalytical Chemistry
https://doi.org/10.1007/s00216-019-01684-7

RESEARCH PAPER

Exonuclease I-assisted fluorescent method for ochratoxin A detection using iron-doped porous carbon, nitrogen-doped graphene quantum dots, and double magnetic separation

Chengke Wang[1] · Rong Tan[1] · Jiangyu Li[1] · Zexiang Zhang[1]

Received: 5 January 2019 / Revised: 29 January 2019 / Accepted: 11 February 2019

Abstract

In this paper, a fluorescent method was developed for ochratoxin A (OTA) detection that uses iron-doped porous carbon (MPC) and aptamer-functionalized nitrogen-doped graphene quantum dots (NGQDs-Apt) as probes. In this method, the adsorbance of the NGQDs-Apt on the MPC due to a π–π interaction between the aptamer and the MPC results in the quenching of the fluorescence of the NGQDs-Apt. However, since OTA interacts strongly with the aptamer, the presence of OTA leads to the detachment of the NGQDs-Apt from the MPC, resulting in the resumption of fluorescence from the NGQDs-Apt. When exonuclease I (Exo I) is also added to the solution, this exonuclease specifically digests the aptamer, leading to the release of the OTA back into the solution. This free OTA then interacts with another MPC–NGQDs-Apt system, inducing the release of more NGQDs into the solution, which enhances the fluorescent intensity compared to that of the system with no Exo I. Utilizing this behavior of OTA in the presence of NGQDs-Apt, it was possible to detect concentrations of OTA ranging from 10 to 5000 nM, with a limit of detection of 2.28 nM. Our method was tested by applying it to the detection of OTA in wheat and corn samples. This method has four advantages: (1) the magnetic porous carbon is easy to prepare, its porosity enhances its loading capacity for NGQDs, it highly efficiently quenches the fluorescence of the NGQDs, and its magnetic properties facilitate the separation of the MPC from other species in solution; (2) applying double magnetic separation decreases the background signal; (3) Exo I digests the free aptamer effectively, which allows the resulting free OTA to induce the release of more NGQDs-Apt, ultimately enhancing the fluorescent signal; and (4) the proposed method presented high sensitivity and a wide linear detection range. This method may prove helpful in food safety analysis and new biosensor development (achieved by using different aptamer sequences to that used in the present work).

Keywords Ochratoxin A · Porous carbon · Magnetic separation · Exonuclease I · Graphene quantum dots

Introduction

Ochratoxin A (OTA) is a type of mycotoxin found in a range of agricultural species, such as corn, wheat, coffee, and fruit. This mycotoxin is harmful to humans and animals, causing carcinogenic, mutagenic, nephrotoxic, and hepatotoxic effects [1–3]. At present, the main methods of detecting OTA include enzyme-linked immunosorbent assay (ELISA), high-performance liquid chromatography (HPLC), liquid chromatography–tandem mass spectrometry (LC-MS), and electrochemical methods [4–8]. Although these methods are highly sensitive, they require expensive antibodies, sophisticated instruments, and professional operators, making them time-consuming and costly to perform and thus inconvenient for practical applications. Therefore, the development of a simple, convenient, low-cost, and sensitive method to detect OTA in agricultural products would be of great benefit.

In recent years, aptamers have been gaining more and more attention from researchers. Aptamers are mainly single-stranded oligonucleotides that are used to recognize particular targets, such as metal ions, mycotoxins, DNA, and proteins [9–12]. Compared with antibodies, aptamers are easier to

Electronic supplementary material The online version of this article (https://doi.org/10.1007/s00216-019-01684-7) contains supplementary material, which is available to authorized users.

✉ Chengke Wang
wangck@ujs.edu.cn

[1] College of Food and Biological Engineering, Jiangsu University, Zhenjiang 212013, China

Published online: 04 March 2019

synthesize and modify, less expensive, more stable, and can be stored for longer [13–15]. Aptamers react with target molecules with good specificity and high affinity. Although they have shown good performance when used to detect many molecules, some improvements to aptamers are still needed; for instance, their sensitivity should be improved, interference from the matrix should be eliminated, the intensity of the background signal should be reduced, and their detection ranges should be broadened [16, 17].

Recently, metal–organic framework (MOF) materials have been receiving a lot of attention due to their tunable structures and compositions as well as their applications in catalysis, chemical sensing, and waste water treatment [18–21]. Compared with traditional hybrid materials, MOFs are easier to synthesize and do not require toxic or expensive precursors such as Cd-, Pb-, and Au/Ag-containing inorganic compounds [22, 23]. Meanwhile, compared with conventional nanomaterial-based fluorescent sensing platforms, MOFs show higher quenching efficiencies towards fluorescent molecules or materials; they achieve this fluorescence quenching through fluorescence resonance energy transfer or nonradiative dipole–dipole coupling [24, 25].

On the other hand, mesoporous or microporous materials have large surface-to-volume ratios, which facilitate their application for small molecule adsorption, loading and transporting drugs, and for biosensing [26–28]. MOFs can be ideal precursors or templates for fabricating metal-containing porous carbon materials via appropriate thermal decomposition treatment [29, 30]. Indeed, highly ordered iron-containing porous carbon with a controllable narrow pore size may be obtained using $Fe(NO_3)_3$ as a raw material; this iron-containing porous carbon (magnetic porous carbon, MPC) could then be used as a magnetic tool to separate different materials [31].

Nitrogen-doped graphene quantum dots (NGQDs) have been widely used as fluorescent nanomaterials in biosensing [32, 33]. Compared with traditional organic dyes or semiconductor quantum dots, they are more easily prepared (simply by heating C- and N-containing precursors), less expensive, and show stronger and more stable fluorescence and better biocompatibility [34, 35]. Therefore, we combined MPC with aptamer-functionalized nitrogen-doped graphene quantum dots (NGQDs-Apt) in a fluorescent assay to detect OTA. To further enhance the signal associated with OTA detection, we also used exonuclease I (Exo I) in our assay, as this exonuclease can degrade single-stranded DNA (ssDNA) in the 3′ to 5′ direction, releasing deoxyribonucleoside 5′-monophosphates in a stepwise manner while leaving 5′-terminal dinucleotides intact; thus, the introduction of Exo I results in the release of free OTA into the solution, which interacts with other MPC–NGQDs-Apt systems, leading to the release of more NGQDs-Apt and thus an enhanced fluorescent signal [36, 37].

In the work reported in the present paper, the structures, compositions, and functional groups of the above materials were carefully studied. We also compared the OTA detection processes that occur in the absence and presence of Exo I, and confirmed that the presence of Exo I enhances the fluorescent signal intensity. Briefly, the MPC binds to the NGQDs-Apt, which results in the quenching of the fluorescence of the NGQDs-Apt. After removing the unreacted NGQDs, OTA is introduced, which interacts with the aptamer to give an aptamer–OTA species and free MPC. When Exo I is also present, the single-stranded aptamer in the aptamer–OTA species is digested by the exonuclease, freeing the OTA and ultimately further enhancing the fluorescent intensity of the solution. After removing the free MPC, the OTA concentration can be determined by measuring the fluorescent intensity. This method was also used to detect OTA in real samples (wheat and corn). The experimental results demonstrated that our method has reasonable sensitivity and selectivity, and may also be modified slightly to allow the detection of other molecules.

Experimental section

Reagents and apparatus

Fumaric acid, $Fe(NO_3)_3 9H_2O$, *N*,*N*-dimethylformamide (DMF), methanol, ammonium citrate, and 1-ethyl-3-(3-dimethylaminopropyl)carbodiimide hydrochloride (EDC) were purchased from Aladdin Reagent Co., Ltd. (Shanghai, China). Zearalenone (ZEN), deoxynivalenol (DON), aflatoxin B1 (AFB1), and fumonisin B1 (FB1) were obtained from Sigma–Aldrich Co. Ltd. (St. Louis, MO, USA). Ochratoxin A (OTA) was purchased from Pribolab Inc. (Singapore). Amino-functionalized OTA aptamer (5′-GATCG GGTGT GGGTG GCGTA AAGGG AGCATC GGACA-C_6H_{12}-NH_2-3′), and Exo I (20 U/μL) were purchased from Sangon Biotechnology Co., Ltd. (Shanghai, China). The wheat and corn samples were purchased from a local supermarket. Double-distilled water (dd H_2O) was used throughout the experiment.

The fluorescence spectra were recorded on a Tecan Infinite 200 PRO microplate reader (Mannedorf, Switzerland). Fourier transform infrared (FT-IR) spectra (4000–400 cm^{-1}) were recorded with a Nicolet IS10 FT-IR spectrometer (Thermo Fisher Scientific, Waltham, MA, USA) by the KBr method. High-resolution transmission electron microscope (HRTEM) micrographs were obtained using a JEM-2100F transmission electron microscope (JEOL, Tokyo, Japan) operated at an accelerating voltage of 200 kV. Scanning electron microscope (SEM) micrographs and energy-dispersive X-ray (EDX) patterns of samples were obtained with a Hitachi (Tokyo, Japan) S-4800II scanning electron microscope

operated at an accelerating voltage of 20 kV. X-ray powder diffraction (XRD) spectra were attained using a Bruker D8 ADVANCE diffractometer (Karlsruhe, Germany) with Cu Kα radiation ($\lambda = 1.5178$ Å, 40 kV × 40 mA). X–ray photoelectron spectra (XPS) were collected using a Thermo ESCALAB250 X-ray photoelectron spectroscope (Thermo Fisher Scientific, Abingdon, UK). The pH values of solutions were adjusted using a Leici PHS-3E pH meter (INESA Scientific Instrument Co., Ltd., Shanghai, China). Images of the solutions were recorded using an S5 IS digital camera (Canon Inc., Tokyo, Japan). Centrifugation was achieved using a WiseSpin CF-10 centrifuge (DAIHAN Scientific, Seoul, Korea). All measurements were carried out at room temperature unless otherwise mentioned.

Preparation of MPC

The MPC was synthesized by a previously reported method with some modifications [38]. Briefly, 462 mg fumaric acid and 1.76 g $Fe(NO_3)_3 9H_2O$ were dissolved in 88 mL DMF and heated at 110 °C for 1 h. Centrifugation was performed to collect the sediments, which were washed with DMF and methanol to remove unreacted material. The resulting products were then further heated to 600 °C at 5 °C/min. This temperature was maintained for 4 h under a N_2 atmosphere. After cooling the powder obtained to room temperature, it was stored at 4 °C.

Preparation of NGQDs

The NGQDs were prepared according to a method defined in a previous report [16]. Briefly, 2 g ammonium citrate were dissolved in 60 mL H_2O and refluxed at 200 °C. After the solution had turned pale yellow, it was heated for another 30 min. After cooling the solution to room temperature, its pH was adjusted to 8.0 and it was stored at 4 °C.

Preparation of NGQDs-Apt

EDC (50 μL; 40 mM) was added to 5 mL of the solution of NGQDs, which was then mixed for 2 min and sonicated for 15 min. After that, 125 μL of an amino-functionalized aptamer (10 μM) were added and the mixture was left to react for 40 min at room temperature. The solution was then centrifuged at 13,500 rpm for 30 min. After removing the supernatant, the sediments were washed with a phosphate buffer (PB) solution (10 mM, pH 7.4), dispersed in PB, and finally stored at 4 °C.

OTA detection process

Twenty microliters of a 0.02 mg/mL MPC solution were mixed with 20 μL of the as-prepared NGQDs-Apt and reacted for 20 min. The products were separated under an external magnetic field and washed with water three times to remove the unreacted NGQDs-Apt. The MPC–NGQDs-Apt complex was redispersed in 135 μL Tris-HCl buffer (10 mM, pH 8.3). Next, 65 μL of a solution containing different amounts of OTA and Exo I were added to the previous solution; this mixture was then incubated for 2 h at room temperature. The solution was separated under an external magnetic field for 10 min and the supernatant was pipetted. Finally, the fluorescence spectrum was recorded using the Tecan Infinite 200 PRO microplate reader.

Real sample preparation and analysis

The real samples were pretreated using previously described methods [39]. Firstly, the wheat and corn samples were crushed to powder that could pass through a 100-mesh sieve. Subsequently, 2 g granules and 0.5 g NaCl were mixed with 5 mL of methanol (80% v/v) for 5 min. The mixture was centrifuged at 10,000 r/min for 10 min, after which extracts of 1 mL supernatant were carefully taken and diluted with 2 mL Tris-HCl (10 mM, pH 7.4). OTA standard solutions with different concentrations were added to the extracts and the OTA was then detected using our proposed method.

Results and discussion

Mechanism for OTA detection

The mechanism for this assay is illustrated in Scheme 1. First, aptamer-conjugated NGQDs and MPC were prepared. Many porous structures formed on the surface of the MPC during the preparation process due to the large surface-to-volume ratio of MPC. π–π stacking interactions between the MPC and the aptamer caused the MPC surface to adsorb the single-stranded DNA, leading to energy transfer from the NGQDs to the MPC and thus quenching the fluorescence of the

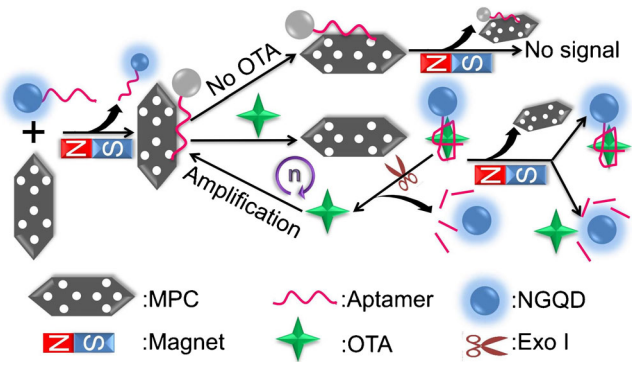

Scheme 1 Schematic of the OTA detection process using MPC, NGQDs-Apt, and double magnetic separation. The illustration is not drawn to scale

NGQDs [31]. Upon performing the first magnetic separation to remove the free (unadsorbed) NGQDs-Apt from the supernatant, the background signal was reduced to a much lower level. However, in the presence of OTA, the NGQDs-Apt formed complexes with OTA due to a specific interaction between the aptamer and OTA [16, 40], which resulted in the desorption of NGQDs-Apt from the MPC surface and consequently the return of the fluorescence. Furthermore, when OTA and Exo I were both present in the solution, the Exo I digested the single-stranded aptamer sequence, causing the ejection of the OTA from the NGQDs-Apt–OTA complex into the solution [36, 41]. The released OTA could then interact with another MPC-NGQDs-Apt complex, leading to a further increase in fluorescence intensity. On the other hand, according to previous reports [42, 43], if OTA is not present in the solution, the MPC in the MPC–NGQDs-Apt complex hinders the approach of Exo I to the aptamer, thus protecting the aptamer from being digested. In other words, our proposed method allows OTA to be detected with enhanced sensitivity since the OTA cycles through multiple aptamer interactions. Finally, a second magnetic separation was conducted to further decrease interference from residual MPC and unreacted MPC–NGQDs-Apt. The supernatant containing the NGQDs was saved and its fluorescence signal was recorded.

Characterization of the MPC and NGQDs-Apt

The morphologies of the MPC and NGQDs were characterized by SEM and HRTEM, respectively. As shown in Fig. 1a, highly mesoporous microsized hexagonal rods were prepared. Meanwhile, the images presented in Fig. 1b show lots of small dots with diameters of 7–8 nm in the NGQDs samples. These experimental results are consistent with previous reports [16, 38]. As shown in Fig. 1c, the MPC was well dispersed in the solution and showed a uniform black color. However, when a bar magnet was placed near to the right hand side of the solution, the solution quickly became colorless, as most of the MPC was magnetically separated (i.e., the black species was attracted to the right hand wall of the centrifuge tube). This confirmed that the prepared materials could be separated through the application of an external magnetic field. These experimental results are consistent with those described in a previous report [31]. The MPC exhibited five typical diffraction peaks at $2\theta = 30°$, 36°, 43°, 57°, and 63°, which could be ascribed to the (220), (311), (400), (511), and (440) crystal planes of γ-Fe_2O_3 (JCPDS card no. 39–1346), as well as two typical diffraction peaks at $2\theta = 44.6°$ and 65°, which could be ascribed to the (110) and (200) crystal planes of α-Fe (JCPDS card no. 06–0696). These results are consistent with previous reports that γ-Fe_2O_3 was formed at high

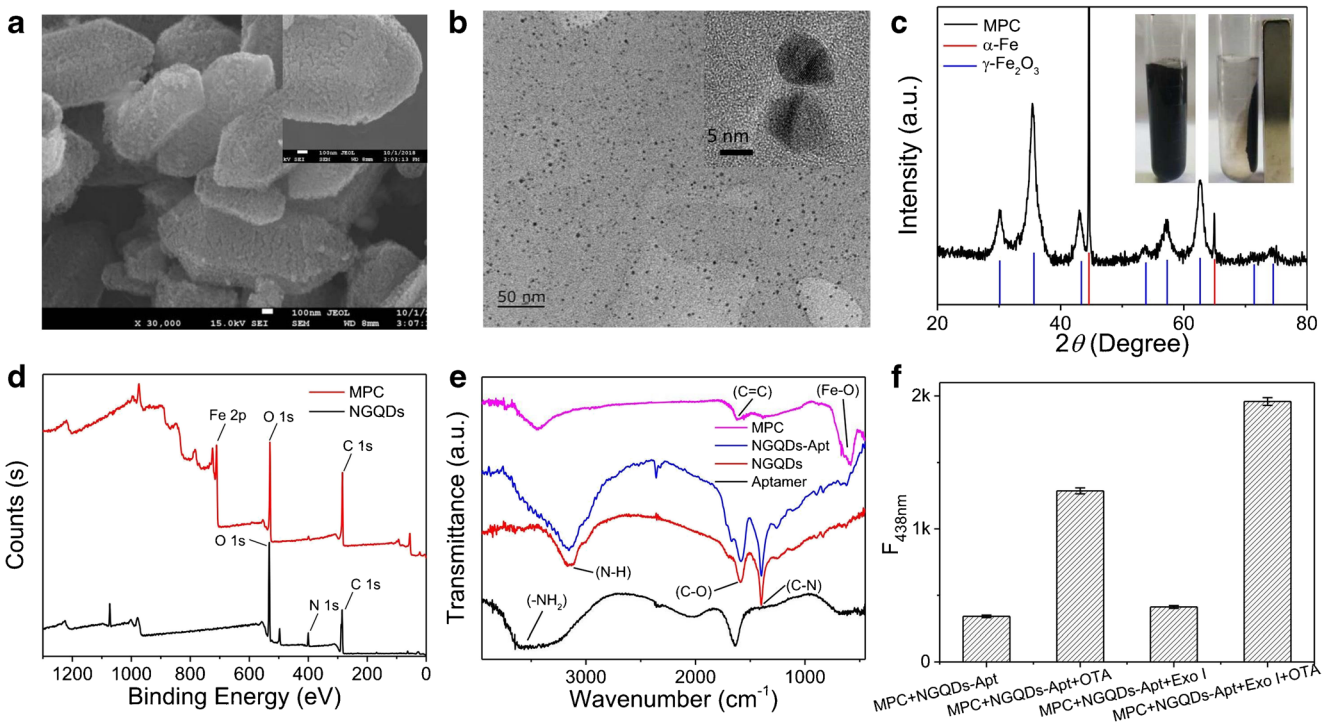

Fig. 1a–f Characterization of different materials. **a** SEM images of the MPC; *scale bars* indicate 100 nm. **b** TEM images of NGQDs-Apt. **c** XRD spectra of the MPC and corresponding standard peaks for γ-Fe_2O_3 and α-Fe; *inset* shows images of the MPC solution before (*left*) and after (*right*) magnetic separation. **d** XPS survey spectra of the MPC and NGQDs samples. **e** FT-IR spectra of the aptamer, NGQDs, NGQDs-Apt, and MPC. **f** The fluorescent signal intensity of the solution at 438 nm (F_{438nm}) in the presence of different species; the concentrations of OTA and Exo I were 500 nM and 140 U, respectively. Each *error bar* represents the relative standard deviation of three experimental results

temperature along with some α-Fe as a by-product, and the percentage of α-Fe in the mixture rose as the temperature was increased [38].

The XPS experimental results indicated that the elements Fe, O, and C were present in MPC, and that O, C, and N were present in NGQDs. In particular, as shown in Fig. S1A of the "Electronic supplementary material" (ESM), two broad peaks at 724 and 710 eV were observed for the MPC material, which were assigned to $Fe2p_{1/2}$ and $Fe2p_{3/2}$, respectively. In addition, the characteristic satellite peak at 719 eV for Fe_2O_3 was also observed, which further confirmed that our prepared MPC consisted of Fe_2O_3 [44]. The EDX results shown in Fig. S1B of the ESM also indicated that the MPC was composed of Fe, O, and C, in good accord with the XPS experimental results.

Furthermore, FT-IR measurements were used to characterize the synthesized materials. As shown in Fig. 1e, an absorption band was observed at 583 cm^{-1}, which was due to Fe–O stretching vibrations in the MPC. A band at 3600 cm^{-1} could be ascribed to NH_2 in the aptamer, while bands at 3100–3300 cm^{-1}, 1500–1750 cm^{-1}, and 1250–1500 cm^{-1} could be assigned to N–H, C–O, and C–N stretching or bending vibrations in NGQDs and NGQDs-Apt, respectively [45]. These results confirmed that Fe-containing MPC and aptamer-functionalized NGQD materials were formed.

Assay feasibility

To demonstrate the feasibility of this assay, the fluorescent signals from solutions containing MPC and NGQDs were recorded. As shown in Fig. S2A of the ESM, the fluorescent intensity of the NGQDs did not change after modification with the aptamer. After adding MPC to the solution of NGQDs, the fluorescent signal was unchanged compared with that of the original solution of NGQDs. However, the fluorescent intensity of the solution was dramatically decreased in the presence of NGQDs-Apt, which may be due to the binding of the NGQDs-Apt to the MPC. These experimental results confirmed our previously mentioned assumptions that π–π stacking between MPC and DNA may result in the binding of NGQD-Apt to the MPC and thus the quenching of the fluorescent signal from NGQDs.

We also compared the fluorescent signal obtained from the NGQDs after adding OTA and separating the solutions twice when Exo I was present and absent. Exo I was added to remove the unreacted NGQDs-Apt and MPC-containing species. As shown in Fig. 1f, the fluorescent signal from the NGQDs-Apt and MPC mixture increased significantly after adding OTA and performing the second magnetic separation, but the signal remained weak after adding Exo I alone, which indicated that the NGQDs-Apt was detached from the MPC and remained in the final solution. It was also observed that the Exo I alone could not interfere with the binding of NGQDs-Apt to the MPC, which is consistent with previous reports that steric hindrance inhibits the hydrolysis of the aptamer on the MPC. However, when the OTA and Exo I were both present in the solution, the fluorescence intensity was even greater than that seen in the presence of OTA alone (no Exo I). These results confirmed our assumption that Exo I can hydrolyze single-stranded DNA which is complexed with OTA, and the OTA released during this hydrolysis can then interact with another aptamer in NGQDs-Apt.

According to a previously published report [40], the interaction of an aptamer with OTA hindered, rather than aided, the enzymatic hydrolysis of the aptamer by Exo I. Although our results are not consistent with that report in terms of the effect of OTA addition on aptamer digestion by Exo I, it is important to note that the aptamer was in a free state before the addition of OTA in the previous work, whereas the aptamer was attached to NGQDs in our work, and those NGQDs were in turn bound to MPC. In the previous work, the interaction of the free OTA with the aptamer led to a conformational change of the aptamer from a random coil to an antiparallel G-quadruplex, which—unlike the random coil conformation—resists digestion by Exo I. On the other hand, in our experiment, when the NGQDs-Apt was bound to the MPC, the conformation of the aptamer was not amenable to digestion by Exo I, whereas the binding of the OTA to the MPC–NGQDs-Apt led to the detachment of NGQDs-Apt–OTA from the MPC, which in turn led to a conformational shift of the aptamer into a form more susceptible to hydrolysis by Exo I. Also, in our method, the OTA released during the digestion of the aptamer was then free to bind to another MPC–NGQDs-Apt system, starting a new cycle of aptamer detachment and digestion. In other words, in our method, each molecule of OTA induces multiple cycles of aptamer digestion, ultimately enhancing the fluorescent signal. Indeed, our experimental results are consistent with previous studies in which graphene was employed to protect the aptamer from digestion by Exo I [42].

Optimization of experimental conditions

In order to determine the optimal experimental conditions for detecting OTA, different amounts of MPC were allowed to interact with the NGQDs-Apt before magnetic separation was performed twice. As shown in Fig. 2a and Fig. S2B of the ESM, the fluorescent intensity of the solution initially increased with increasing MPC, presumably because more MPC–NGQDs-Apt complexes were created, ultimately leading to a stronger fluorescent signal after the addition of OTA. However, as the amount of MPC exceeded 0.02 mg/mL, the excess MPC began to hinder the ability of OTA to interact with NGQDs-Apt. Therefore, the increase in fluorescent intensity obtained upon the addition of OTA began to drop as the MPC was increased at levels above 0.02 mg/mL. We also

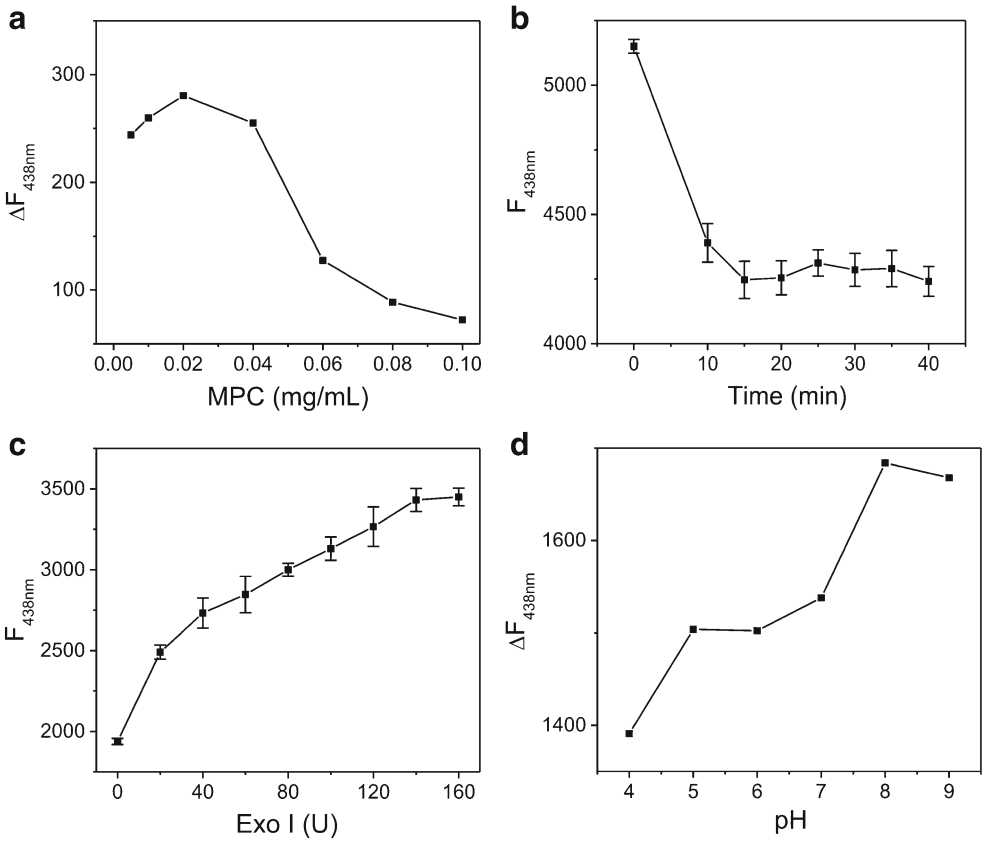

Fig. 2a–d Optimizing the experimental conditions. **a** Plot of the change in fluorescence upon adding 200 nM OTA (F_{438nm}) versus the concentration of MPC. **b** Plot of the variation in F_{438nm} from the NGQDs-Apt over time following the addition of 20 μL of 0.02 mg/mL MPC. **c** Plot of the variation in F_{438nm} after double magnetic separation as a function of the amount of Exo I added. **d** Plot of the change in fluorescence F_{438nm} following the addition of 500 nM OTA as a function of pH. Each *error bar* represents the relative standard deviation of three experimental results

investigated the variation in fluorescent intensity over time following the addition of MPC (Fig. 2b). The fluorescent intensity initially decreased rapidly for the first 10 min following MPC addition, but the intensity then leveled out. The optimal concentration of Exo I to hydrolyze the single-stranded aptamer in the NGQDs-Apt was also studied, as shown in Fig. 2c and Fig. S2C in the ESM. The final fluorescent intensity of the solution after two magnetic separations was observed to increase with increasing Exo I in the solution until more than 140 U Exo I had been added. Finally, the optimal pH of the solutions was investigated, as shown in Fig. 2d and Fig. S2D of the ESM. At pH values from 4 to 9, the fluorescent signal intensity of the solution in the presence of OTA was always higher than that in the absence of OTA, and the increase in fluorescent intensity upon OTA addition was greatest when the pH was 8.0. This may be because the interaction of OTA with the aptamer is strongest at this pH value [17, 39]. Therefore, in subsequent experiments, 0.02 mg/mL MPC were allowed to interact with 20 μL of NGQDs-Apt for 20 min at a solution pH of 8, and the amount of Exo I added was 140 U.

Detection of OTA

Under optimal experimental conditions, we investigated the characteristics of OTA detection using our proposed method. In the non-enzyme-assisted version of the method, MPC was added to quench the fluorescent intensity of the NGQDs-Apt; the unreacted NGQDs-Apt were removed by applying an external magnetic field; the MPC–NGQDs-Apt complex was allowed to interact with OTA, thus releasing NGQDs-Apt into the solution; a second magnetic separation was then performed to remove the free MPC and therefore decrease the background signal; finally, the fluorescence from the NGQDs-containing supernatant was measured. In the enzyme-assisted measurements, OTA and Exo I were added simultaneously to further hydrolyze the detached NGQDs-Apt–OTA complex; the resulting free OTA was then able to bind to another MPC–NGQDs-Apt system, leading to more free NGQDs in the final solution after the second magnetic separation. This enhances the fluorescent signal.

As shown in Fig. 3a, in the absence of Exo I, the fluorescent signal intensity increased as the concentration of OTA was ramped up from 20 to 5000 nM, and the wavelength at which maximum intensity was obtained was 438 nm. Indeed, Fig. 3c shows that the fluorescent intensity at 438 nm (F_{438nm}) increased linearly as the concentration of OTA was increased from 20 to 5000 nM; the equation for this linear correlation was $F_{438nm} = 1.54C_{OTA} + 368.1$ ($R^2 = 0.996$), where C_{OTA} refers to the concentration of OTA (nM). The limit of detection (LOD) was determined as three times the standard deviation σ of the blank (i.e., 2.08) divided by the slope of the calibration

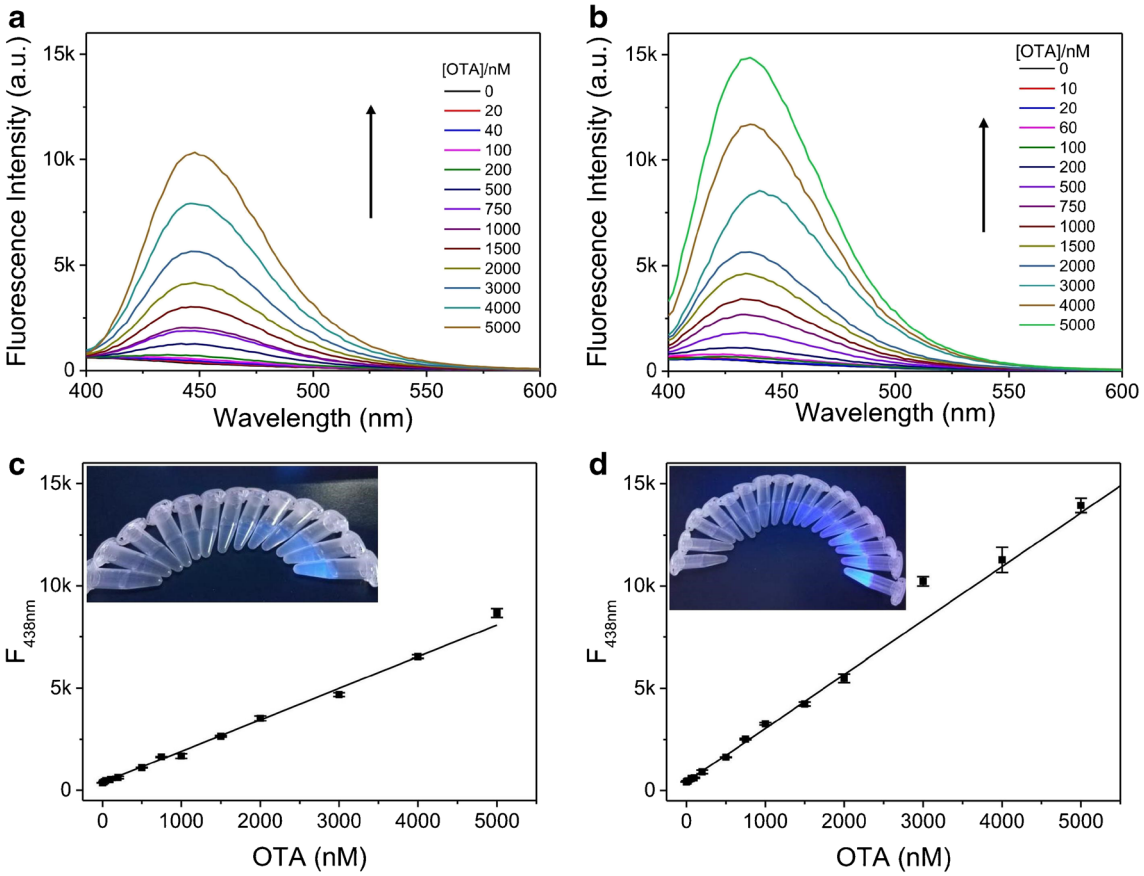

Fig. 3a–d Investigating the characteristics of OTA detection using the proposed method. Fluorescence spectra obtained from various test solutions in the presence of different concentrations of OTA but in the absence (**a**) or in the presence of (**b**) of 140 U Exo I are shown. Plots of F_{438nm} from the solutions as a function of the concentration of OTA but in the absence (**c**) or in the presence (**d**) of Exo I are also presented. Each *error bar* represents the relative standard deviation of three experimental results. The *insets* of **c** and **d** show images of the solutions fluorescing under ultraviolet light (365 nm); the concentrations of OTA in the solutions increase from left to right from 0 to 5000 nM

curve (i.e., 1.54), which gave a value of 4.05 nM. The limit of quantification (LOQ) was calculated as 10σ, which corresponded to 13.5 nM. The images at the top of Fig. 3c also indicate that the fluorescent signal increased with increasing OTA concentration, which is consistent with the fluorescence spectra in Fig. 3a.

We also investigated the OTA detection characteristics of our proposed method in the presence of Exo I, as shown in Fig. 3b. At the same concentrations of OTA, the fluorescent signal intensity in the solution with Exo I was higher than that of the solution without Exo I, confirming that Exo I was able to hydrolyze the NGQDs-Apt–OTA complex, and that the released OTA then interacted with another MPC–NGQDs-Apt system, ultimately leading to the dispersal of more NGQDs in the detection solution. We again examined the linearity of F_{438nm} with respect to the concentration of OTA, as shown in Fig. 3d. F_{438nm} was observed to increase linearly as the concentration of OTA rose from 10 to 5000 nM; the equation for the linear correlation was $F_{438nm} = 2.63C_{OTA} + 410.8$ ($R^2 = 0.999$). The limit of detection (LOD) was determined as three times the standard deviation σ of the blank (i.e., 2.00) divided by the slope of the calibration curve (i.e., 2.63), which gave a value of 2.28 nM. The LOQ was calculated as 10σ, which corresponded to a value of 7.6 nM. Compared with the system without Exo I, the sensitivity was enhanced, and the linear detection range was also wider. From the inset images shown in Fig. 3d, it is clear that the fluorescent signal intensity was also increased compared to the system without Exo I, highlighting the important role of Exo I in the OTA detection process of our proposed method. In fact, in this experiment, increasing the OTA concentration above 5000 nM led to a further increase in fluorescent intensity (data not shown here); however, considering the actual application of this method (i.e., the OTA concentrations in real samples are rarely over 5000 nM), and the fact that the absorptions of such solutions were too high to detect (> 4.0, which was beyond the detection range of the instrument), the maximum concentration of OTA considered in this experiment was 5000 nM. The European Commission set the maximum level of OTA at

Table 1 Comparison of this fluorescent method with previously reported methods

Method	Linear range (nM)	LOD (nM)	Reference
Colorimetric	20–625	20.00	[46]
Electrochemical	24–120	24.00	[47]
Fluorescent	20–500	16.50	[40]
Fluorescent	20–500	17.20	[48]
Fluorescent	6–500	3.00	[49]
Fluorescent	50–500	18.70	[50]
Fluorescent	4.96–49.6	4.96	[51]
Fluorescent (no Exo I)	10–5000	4.05	This work
Fluorescence (Exo I)	10–5000	2.28	This work

5 μg/kg (12.5 nM) for raw cereal grain and at 10 μg/kg (25 nM) for soluble coffee (Commission Regulation nos. 123/2005 and 466/2001, respectively) [46], so our method could be used for OTA detection in actual samples.

As shown in Table 1, our Exo I-assisted fluorescent method utilizing double magnetic separation exhibited reasonable sensitivity, as the LOD was equal to or lower than those of previous published methods. In addition, our method had a wide linear detection range (three orders of magnitude). These advantages may derive from the substantial decrease in the background signal due to the application of double magnetic separation, as well as the large surface-to-volume ratio of the MPC, which enhanced its loading efficiency for NGQDs-Apt and led to the efficient quenching of the fluorescence of the NGQDs. In addition, Exo I efficiently hydrolyzed the single-stranded DNA when the aptamer was detached from the MPC; this in turn led to the release of free OTA, which was then able to trigger the release of more NGQDs-Apt from MPC, further enhancing the detected fluorescent intensity.

Specificity evaluation

In order to evaluate the specificity of the proposed method, different mycotoxins were added to the solution and the resulting fluorescent signals were recorded using our proposed method, as shown in Fig. 4. Under the same experimental conditions, the fluorescent intensity of the solution increased only if OTA was present; interference from other mycotoxins in the OTA detection was minor or nonexistent. These experimental results indicate that our proposed method presents reasonable selectivity for OTA, which may be attributed to the high specificity and binding affinity of OTA for the aptamer.

OTA detection in wheat and corn

It is important to be able to detect OTA in real samples such as wheat and corn, as they are easily contaminated by OTA. Therefore, a standard addition method was utilized to verify the applicability of the proposed method to real samples. The results are shown in Table 2. Four different concentrations (400, 600, 750, and 1000 nM) of OTA were added to the wheat and corn samples, and the OTA was then detected using our proposed method. The average recoveries achieved with this method ranged from 87% to 110%, and the relative standard deviation (RSD) was less than 6.08%. These results indicate that our method could be used to determine the OTA levels in real samples. Since satisfactory results were obtained when using OTA-spiked foodstuffs, we speculate that this method could also be effectively applied to detect the contamination of real foodstuffs, which would make the proposed method rather valuable. However, in our present work,

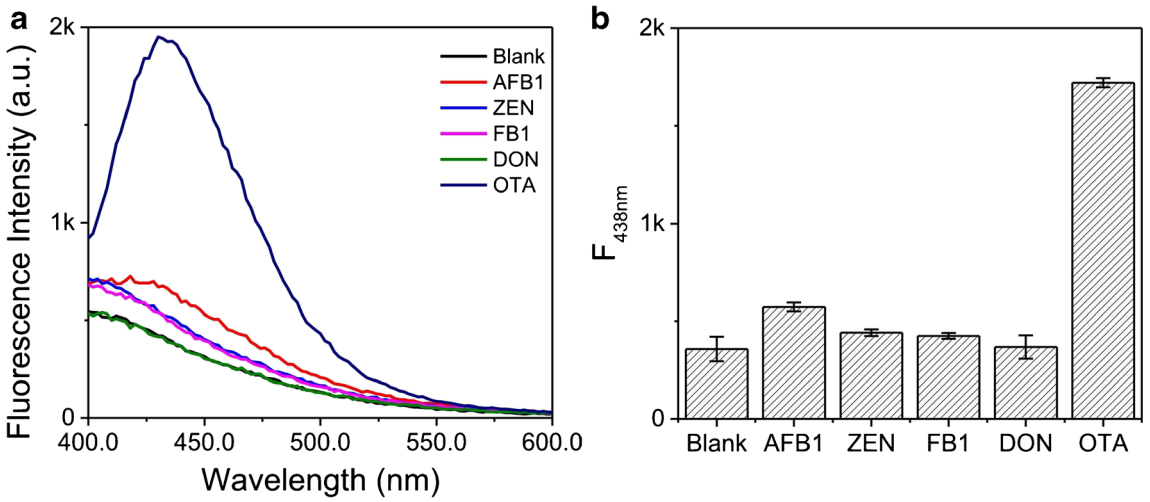

Fig. 4a–b Investigating the selectivity of the proposed method. **a** Fluorescence spectra of various test solutions in the absence and presence of different mycotoxins at a concentration of 500 nM. **b** The F_{438nm} values of the solutions listed in **a**. Each *error bar* represents the relative standard deviation of three experimental results

Table 2 Determination of OTA concentrations in wheat and corn samples (n = 3) using our proposed method

Sample	Added concentration of OTA (nM)	Mean determined concentration of OTA ± SD (nM)	Recovery (%)	RSD (%)
Wheat 1	400	378.26 ± 24.33	94.57	6.08
Wheat 2	600	564.00 ± 32.61	94.00	5.44
Wheat 3	750	649.95 ± 43.94	86.66	5.86
Wheat 4	1000	991.37 ± 42.73	99.14	4.27
Corn 1	400	384.25 ± 12.46	96.06	3.12
Corn 2	600	594.28 ± 8.63	99.05	1.44
Corn 3	750	740.24 ± 20.05	98.70	2.67
Corn 4	1000	1099.14 ± 15.16	109.9	1.52

contaminated foodstuffs were not easy to obtain. In subsequent studies, we will continue to study the application of this method to real agricultural products contaminated with OTA by cooperating with other groups or by culturing the foodstuffs in a humified environment; this work is already in progress in our lab.

Conclusions

In conclusion, we have developed a fluorescent method for detecting OTA using MPC, NGQDs, and double magnetic separation. The MPC acts as both a quenching agent and a separation material with a porous surface and a large surface-to-volume ratio. The background signal during detection was decreased by applying magnetic separation twice in order to remove unreacted NGQDs and free MPC. The fluorescent intensity was enhanced by introducing Exo I into the system, as the Exo I hydrolyzes the aptamer–OTA complex, which releases the OTA and thus frees it to interact with another NGQDs-Apt, ultimately increasing the OTA detection sensitivity of the method. OTA was detected with a limit of detection of 2.28 nM using the proposed method, and its linear detection range was 10–5000 nM. This method could also be used to detect OTA in real samples of wheat and corn. It should prove useful for food safety analysis and may facilitate the development of other biosensors with different aptamer sequences.

Acknowledgments This study was funded by the National Natural Science Foundation of China (no. 21305032), the China Postdoctoral Science Foundation (no. 2014 M551522), Jiangsu Planned Projects for Postdoctoral Research Funds (no. 1402073B), and Hong Kong Scholar Program (no. XJ2017008).

Compliance with ethical standards

Conflict of interest The authors declare that they have no conflict of interest.

References

1. Ostry V, Malir F, Toman J, Grosse Y. Mycotoxins as human carcinogens—the IARC monographs classification. Mycotoxin Res. 2017;33(1):65–73.
2. Liew WPP, Mohd-Redzwan S. Mycotoxin: its impact on gut health and microbiota. Front Cell Infect Microbiol. 2018;8:60.
3. Lee HJ, Ryu D. Worldwide occurrence of mycotoxins in cereals and cereal-derived food products: public health perspectives of their co-occurrence. J Agric Food Chem. 2017;65(33):7034–51.
4. Zhang YY, Pei F, Fang Y, Li P, Zhao Y, Shen F, et al. Comparison of concentration and health risks of 9 fusarium mycotoxins in commercial whole wheat flour and refined wheat flour by multi-IAC-HPLC. Food Chem. 2019;275:763–9.
5. Tang ZW, Wang XR, Lv JW, Hu XR, Liu X. One-step detection of ochratoxin a in cereal by dot immunoassay using a nanobody-alkaline phosphatase fusion protein. Food Control. 2018;92:430–6.
6. Sun ZC, Lv JW, Liu X, Tang ZW, Wang XR, Xu Y, et al. Development of a nanobody-AviTag fusion protein and its application in a streptavidin-biotin-amplified enzyme-linked immunosorbent assay for ochratoxin A in cereal. Anal Chem. 2018;90(17):10628–34.
7. Majdinasab M, Zareian M, Zhang Q, Li PW. Development of a new format of competitive immunochromatographic assay using secondary antibody-europium nanoparticle conjugates for ultrasensitive and quantitative determination of ochratoxin A. Food Chem. 2019;275:721–9.
8. Jalalvand AR. Fabrication of a novel and high-performance amperometric sensor for highly sensitive determination of ochratoxin A in juice samples. Talanta. 2018;188:225–31.
9. Majdinasab M, Hayat A, Marty JL. Aptamer-based assays and aptasensors for detection of pathogenic bacteria in food samples. TRAC—Trend Anal Chem. 2018;107:60–77.
10. Farzin L, Shamsipur M, Sheibani S. A review: aptamer-based analytical strategies using the nanomaterials for environmental and human monitoring of toxic heavy metals. Talanta. 2017;174:619–27.
11. Deng B, Lin YW, Wang C, Li F, Wang ZX, Zhang HQ, et al. Aptamer binding assays for proteins: the thrombin example—a review. Anal Chim Acta. 2014;837:1–15.
12. Cunha I, Biltes R, Sales MGF, Vasconcelos V. Aptamer-based biosensors to detect aquatic phycotoxins and cyanotoxins. Sensors. 2018;18(7):2367.
13. Zhou W, Huang PJ, Ding J, Liu J. Aptamer-based biosensors for biomedical diagnostics. Analyst. 2014;139(11):2627–40.
14. Mok W, Li YF. Recent progress in nucleic acid aptamer-based biosensors and bioassays. Sensors. 2008;8(11):7050–84.

15. Amaya-Gonzalez S, de los Santos Alvarez N, Miranda-Ordieres AJ, Lobo-Castanon MJ. Aptamer-based analysis: a promising alternative for food safety control. Sensors. 2013;13(12):16292–311.
16. Wang CK, Tan R, Chen D. Fluorescence method for quickly detecting ochratoxin A in flour and beer using nitrogen doped carbon dots and silver nanoparticles. Talanta. 2018;182:363–70.
17. Wang CK, Chen D, Wang QQ, Wang QX. Aptamer-based resonance light scattering for sensitive detection of acetamiprid. Anal Sci. 2016;32(7):757–62.
18. Wu YQ, Qiu XC, Liang F, Zhang QK, Koo A, Dai YN, et al. A metal-organic framework-derived bifunctional catalyst for hybrid sodium-air batteries. Appl Catal B—Environ. 2019;241:407–14.
19. Nguyen TN, Ebrahim FM, Stylianou KC. Photoluminescent, upconversion luminescent and nonlinear optical metal-organic frameworks: from fundamental photophysics to potential applications. Coord Chem Rev. 2018;377:259–306.
20. Gupta V, Tyagi S, Paul AK. Development of biocompatible iron–carboxylate metal organic frameworks for pH-responsive drug delivery application. J Nanosci Nanotechnol. 2019;19(2):646–54.
21. Gao XY, Zhu G, Zhang XJ, Hu T. Porous carbon materials derived from in situ construction of metal-organic frameworks for high-performance sodium ions batteries. Microporous Mesoporous Mater. 2019;273:156–62.
22. Nadar SS, Rathod VK. Magnetic-metal organic framework (magnetic-MOF): a novel platform for enzyme immobilization and nanozyme applications. Int J Biol Macromol. 2018;120:2293–302.
23. Ajoyan Z, Marino P, Howarth AJ. Green applications of metal-organic frameworks. CrystEngComm. 2018;20(39):5899–912.
24. Zhu SY, Yan B. A novel sensitive fluorescent probe of $S_2O_8^{2-}$ and Fe^{3+} based on covalent post-functionalization of a zirconium(IV) metal-organic framework. Dalton Trans. 2018;47(33):11586–92.
25. Xu PP, Liao GF. A novel fluorescent biosensor for adenosine triphosphate detection based on a metal-organic framework coating polydopamine layer. Materials. 2018;11(9):1616.
26. Yu FQ, Zhou H, Shen Q. Modification of cobalt-containing MOF-derived mesoporous carbon as an effective sulfur-loading host for rechargeable lithium-sulfur batteries. J Alloys Compd. 2019;772:843–51.
27. Wu ZL, Sun LP, Zhou Z, Li Q, Huo LH, Zhao H. Efficient nonenzymatic H_2O_2 biosensor based on ZIF-67 MOF derived co nanoparticles embedded N-doped mesoporous carbon composites. Sensors Actuators B Chem. 2018;276:142–9.
28. Kang JS, Kang J, Chung DY, Son YJ, Kim S, Kim S, et al. Tailoring the porosity of MOF-derived N-doped carbon electrocatalysts for highly efficient solar energy conversion. J Mater Chem A. 2018;6(41):20170–83.
29. Li BY, Chrzanowski M, Zhang YM, Ma SQ. Applications of metal-organic frameworks featuring multi-functional sites. Coord Chem Rev. 2016;307:106–29.
30. Liu DX, Zou DT, Zhu HL, Zhang JY. Mesoporous metal–organic frameworks: synthetic strategies and emerging applications. Small. 2018;14(37):1801454.
31. Tan HL, Tang GE, Wang ZX, Li Q, Gao J, Wu SM. Magnetic porous carbon nanocomposites derived from metal-organic frameworks as a sensing platform for DNA fluorescent detection. Anal Chim Acta. 2016;940:136–42.
32. Zhu ZM, Lin XY, Wu LN, Zhao CF, Zheng YJ, Liu AL, et al. "Switch-on" fluorescent nanosensor based on nitrogen-doped carbon dots-MnO_2 nanocomposites for probing the activity of acid phosphatase. Sensors Actuators B Chem. 2018;274:609–15.
33. Ganganboina AB, Doong RA. Functionalized N-doped graphene quantum dots for electrochemical determination of cholesterol through host-guest inclusion. Microchim Acta. 2018;185(11):526.
34. Hai X, Feng J, Chen XW, Wang JH. Tuning the optical properties of graphene quantum dots for biosensing and bioimaging. J Mater Chem B. 2018;6(20):3219–34.
35. Gao J, Zhu MM, Huang H, Liu Y, Kang ZH. Advances, challenges and promises of carbon dots. Inorg Chem Front. 2017;4(12):1963–86.
36. Lin CY, Zheng HX, Huang YY, Chen ZL, Luo F, Wang J, et al. Homogeneous electrochemical aptasensor for mucin 1 detection based on exonuclease I-assisted target recycling amplification strategy. Biosens Bioelectron. 2018;117:474–9.
37. Chen XX, Hong F, Cao YT, Hu FT, Wu YX, Wu DZ, et al. A microchip electrophoresis-based assay for ratiometric detection of kanamycin by R-shape probe and exonuclease-assisted signal amplification. Talanta. 2018;189:494–501.
38. Lee HJ, Cho W, Lim E, Oh M. One-pot synthesis of magnetic particle-embedded porous carbon composites from metal-organic frameworks and their sorption properties. Chem Commun. 2014;50(41):5476–9.
39. Wang C, Dong X, Liu Q, Wang K. Label-free colorimetric aptasensor for sensitive detection of ochratoxin A utilizing hybridization chain reaction. Anal Chim Acta. 2015;860:83–8.
40. Lv L, Li D, Liu R, Cui C, Guo Z. Label-free aptasensor for ochratoxin A detection using SYBR gold as a probe. Sensors Actuators B Chem. 2017;246:647–52.
41. Zhang JJ, Sun Y, Lu JZ. A novel bioluminescent detection of exonuclease I activity based on terminal deoxynucleotidyl transferase-mediated pyrophosphate release. Luminescence. 2018;33(7):1157–63.
42. Pu Y, Zhu Z, Han D, Liu HX, Liu J, Liao J, et al. Insulin-binding aptamer-conjugated graphene oxide for insulin detection. Analyst. 2011;136(20):4138–40.
43. Wu YR, Phillips JA, Liu HP, Yang RH, Tan WH. Carbon nanotubes protect DNA strands during cellular delivery. ACS Nano. 2008;2(10):2023–8.
44. Ma Y, Ji G, Lee JY. Synthesis of mixed-conducting carbon coated porous γ-Fe_2O_3 microparticles and their properties for reversible lithium ion storage. J Mater Chem. 2011;21(34):13009–14.
45. Lin-Vien D, Colthup NB, Fateley WG, Grasselli JG. Chapter 10: Compounds containing $–NH_2$, –NHR, and $–NR_2$ groups. The handbook of infrared and Raman characteristic frequencies of organic molecules. San Diego: Academic Press; 1991. p. 155–78.
46. Yang C, Wang Y, Marty JL, Yang XR. Aptamer-based colorimetric biosensing of ochratoxin A using unmodified gold nanoparticles indicator. Biosens Bioelectron. 2011;26(5):2724–7.
47. Radi A-E, Muñoz-Berbel X, Cortina-Puig M, Marty J-L. An electrochemical immunosensor for ochratoxin A based on immobilization of antibodies on diazonium-functionalized gold electrode. Electrochim Acta. 2009;54(8):2180–4.
48. Lv L, Cui C, Liang C, Quan W, Wang S, Guo Z. Aptamer-based single-walled carbon nanohorn sensors for ochratoxin A detection. Food Control. 2016;60:296–301.
49. Wang R, Xiang Y, Zhou X, Liu LH, Shi H. A reusable aptamer-based evanescent wave all-fiber biosensor for highly sensitive detection of ochratoxin A. Biosens Bioelectron. 2015;66:11–8.
50. Sheng L, Ren J, Miao Y, Wang J, Wang E. PVP-coated graphene oxide for selective determination of ochratoxin A via quenching fluorescence of free aptamer. Biosens Bioelectron. 2011;26(8):3494–9.
51. Bueno D, Muñoz R, Marty JL. Fluorescence analyzer based on smartphone camera and wireless for detection of ochratoxin A. Sensors Actuators B Chem. 2016;232:462–8.